RSC Advances

PAPER

View Article Online
View Journal | View Issue

Cite this: *RSC Adv.*, 2023, **13**, 14224

Electroactive nanofibrous membrane with temperature monitoring for wound healing†

Liguo Yang,‡[a] Chenglin Li,‡[b] Xuefang Wang,[a] Xiangyan Zhang,*[c] Yongxin Li,*[c] Shangpeng Liu[a] and Jiwei Li *[ad]

Developing functional dressings for promoting cellular activities and monitoring the healing progress is receiving increasingly widespread attention. In this study, Ag/Zn electrodes were deposited on the surface of a polylactic acid (PLA) nanofibrous membrane which can mimic the extracellular matrix. When wetted by wound exudate, the Ag/Zn electrodes could generate an electric stimulation (ES), promoting the migration of fibroblasts that heal wounds. Moreover, the Ag/Zn@PLA dressing showed excellent antibacterial activity against *E. coli* (95%) and *S. aureus* (97%). The study found that the electrostatic (ES) effect and the release of metal ions mainly contribute to the wound healing properties of Ag/Zn@PLA. *In vivo* mouse models demonstrated that Ag/Zn@PLA could promote wound healing by improving re-epithelialization, collagen deposition, and neovascularization. Additionally, the integrated sensor within the Ag/Zn@PLA dressing can monitor the wound site's temperature in real-time, providing timely information on wound inflammatory reactions. Overall, this work suggests that combining electroactive therapy and wound temperature monitoring may provide a new strategy for designing functional wound dressings.

Received 14th March 2023
Accepted 4th May 2023

DOI: 10.1039/d3ra01665j

rsc.li/rsc-advances

1. Introduction

As the human body's largest organ, the skin is the protective barrier against the external environment.[1,2] Once the skin suffers from serious damage, acute or chronic wounds will severely affect people's health and life.[3,4] Therefore, due to the increasing incidence of skin injuries, there is an urgent need for functional wound dressings.

Endogenous electric field, which could promote cell proliferation and migration, is crucial to skin regenerative activities and wound repair.[5,6] Recently, various electroactive wound dressings have been developed, including conductive nanofibers,[7,8] conductive hydrogels,[9,10] piezoelectric patches,[11,12] and micro-battery dressings.[13,14] Among them, the micro-battery dressings impregnate electrochemically coupled metals on the fabric, and electric stimulation (ES) is generated when a conductive medium (wound's exudate, blood, *etc.*) wets the coupled metals on the matrix.[15,16] The generated weak ES can promote wound healing by supporting cell migration, improving epithelization, and disrupting biofilm formation.[17,18] However, most reported micro-battery dressings were prepared from micron fiber-based fabrics or nonwovens, which is not conducive to cell migration and proliferation during wound healing.

The ability to mimic an extracellular matrix's (ECM) structure, the good mechanical performance, and the inherently high surface-to-volume ratio make nanofibrous membranes suitable for various biomedical applications.[19–21] Especially, nanofibrous membranes could recapitulate the fibrous architecture of native tissue microenvironments crucial for wound repair, and increasingly nanofibrous membranes have been applied in wound dressings.[22,23] Moreover, the temperature is one of the important indicators for assessing wound status, and quantitative skin temperature measurements around wounds can help wound care practitioners identify deep or disseminated infections early.[24,25] Therefore, it is urgently needed to construct a bioelectric nanofibrous dressing with electrical stimulating wound healing properties and simultaneously for dynamic wound temperature monitoring.

In this study, the Ag/Zn electrodes were sputtered on the surface of PLA nanofibrous membranes to prepare an electroactive wound dressing (Ag/Zn@PLA) (Fig. 1a). The Ag/Zn electrode was set as a circular ring to facilitate generating electrical stimulation from the wound surrounding to the center. Then

[a]*College of Textiles and Clothing, Industrial Research Institute of Nonwovens and Technical Textiles, Qingdao University, Qingdao, 266071, China. E-mail: jiweili@qdu.edu.cn*

[b]*Department of Biochemistry and Microbiology, Qingdao University Medical College, Qingdao University, Qingdao, 266003, China*

[c]*Department of Pathology, Department of Vascular Surgery, The Affiliated Hospital of Qingdao University, Qingdao University, Qingdao, 266003, China. E-mail: feige5552006@126.com; li.yongxin@outlook.com*

[d]*Shandong Center for Engineered Nonwovens, Qingdao, 266071, China*

† Electronic supplementary information (ESI) available. See DOI: https://doi.org/10.1039/d3ra01665j

‡ These authors contributed equally.

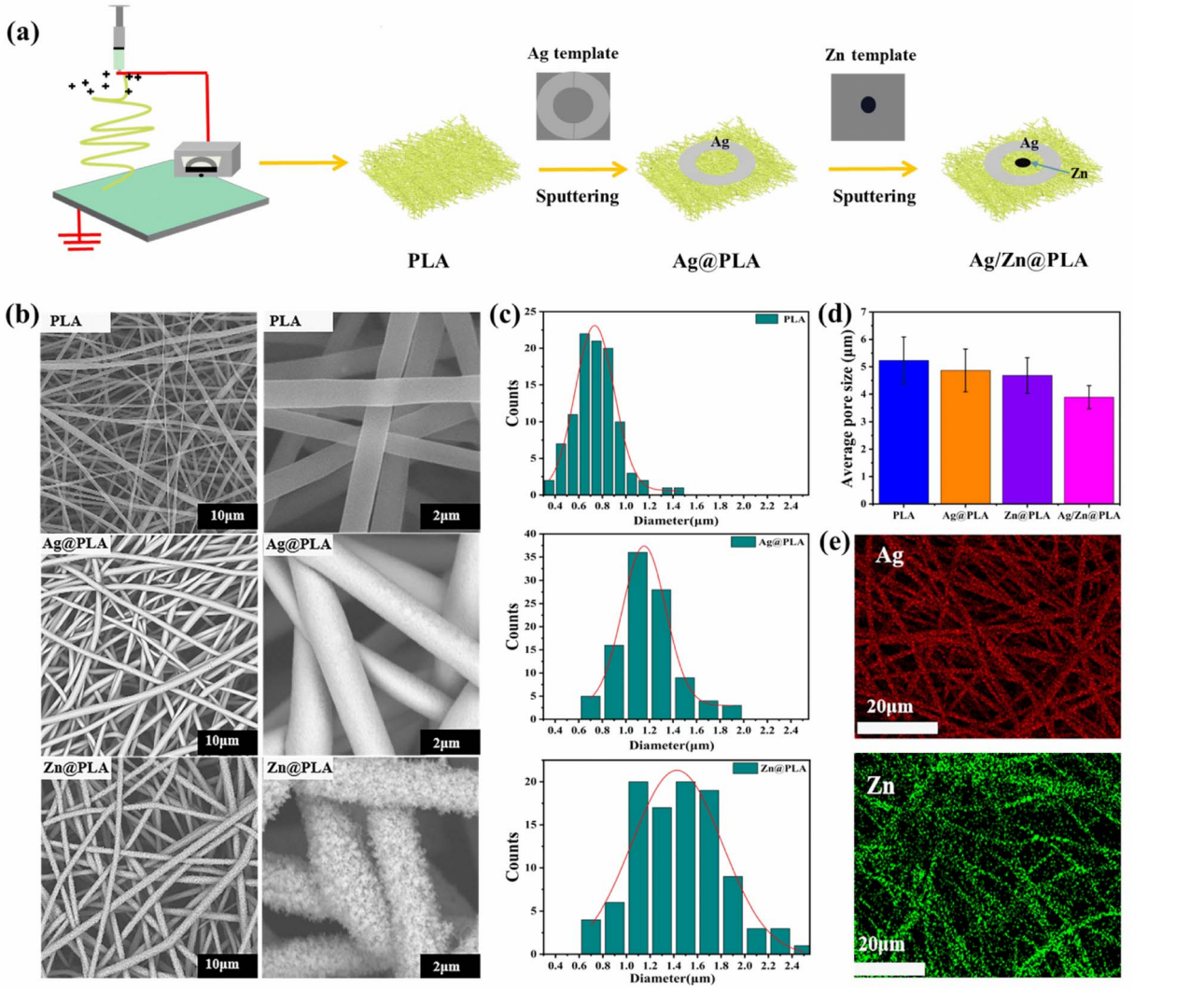

Fig. 1 (a) Schematic illustration of the fabrication process of the Ag/Zn@PLA dressing. (b) SEM images of the PLA, Ag@PLA, and Zn@PLA. (c) Diameter distribution of the PLA, Ag@PLA, and Zn@PLA. (d) The average pore size of the PLA, Ag@PLA, and Zn@PLA. (e) EDX spectra of the Ag deposited PLA (red, Ag element) and Zn deposited PLA (green, Zn element).

the miniature sensor DHT11 is integrated into the Ag/Zn@PLA dressing to achieve real-time temperature monitoring of the wound site. The structure, morphology, mechanical properties, and antibacterial properties of the resulting Ag/Zn@PLA were systematically investigated. Furthermore, the wound healing ability and biocompatibility of Ag/Zn@PLA were evaluated by *in vitro* and *in vivo* experiments to verify its suitability for wound healing applications.

2. Materials and methods

2.1. Materials

The polylactic acid was purchased from Solvay Company (US). Both the Ag (Φ 50.8 × 5 mm, 99.99%) and Zn (Φ 50.8 × 5 mm, 99.99%) targets were purchased from ZhongNuo Advanced Material (Beijing) Technology Co., Ltd. The template used for sputtering is composed of polymethyl methacrylate (PMMA) cut to a specific shape. The *Staphylococcus aureus* (CMCC 26003) and *Escherichia coli* (ATCC 25922) were purchased from Shanghai Luwei Technology Co., Ltd. Nutrient agar was purchased from Beijing Luqiao Technology Co., Ltd., China. The 4′,6-diamidino-2-phenylindole (DAPI) was purchased from Shanghai Abocon Trading Co., Ltd. (China). Primary human embryonic lung fibroblasts (HELF) were stored in the laboratory and cryopreserved in a −80 °C freezer. Cultures were expanded with DMEM/F-12 (2037140, Biological Industries) containing 10% fetal bovine serum (11011-8611, Every Green) in a 37 °C, 5% CO_2 incubator. If not explicitly mentioned, the other reagents used in this study were all analytical grade and purchased commercially from Qingdao, China.

2.2. Preparation of PLA nanofibrous membrane

The 8 wt% PLA spinning solution was obtained by dissolving 1.6 g PLA in 3.68 g DMF and 14.72 g DCM, stirring for 8 hours at room temperature. The prepared electrospinning solution was

placed into a 10 mL syringe at a flow rate of 1 mL h^{-1}, a voltage of 20 kV, and a die-to-collector distance of 10 cm.

2.3. Preparation of Ag/Zn@PLA dressing

The magnetron sputtering of PLA was according to our previous works.[26,27] Firstly, a circular layer of silver oxide (Ag electrode) was sputtered on the PLA fiber membrane by gaseous deposition with a ratio of oxygen to argon of 1 : 1 and a flow rate of 15 standard cubic centimeters per minute (sccm). The sputtering power was kept at 60 W, and the sputtering time was 15 min. The resulting Ag deposited PLA was labeled as Ag@PLA. Then the second step places Ag@PLA in an argon environment and sputters with a zinc target to prepare Ag/Zn@PLA. During this process, zinc oxide will not be generated as no oxygen.

2.4. Characterizations

The micromorphology was observed by a scanning electron microscope (SEM) (TESCAN VEGA3, China) equipped with energy-dispersive X-ray spectroscopy (EDS). The Image J software calculated the average diameter of the fibers. The water contact angle was measured with a contact angle goniometer (JY-PH, Chengde Jinhe Instruments, China) equipped with a digital camera. Thermogravimetric analysis (TGA) was performed on a TG209F3 instrument from room temperature to 700 °C with a heating rate of 10 °C min^{-1} in a nitrogen flow.

2.5. Antibacterial test

2.5.1. The agar diffusion method. Nutrient agar was used as the bacterial medium. First, customized samples (diameter = 2.5 cm) were kept in Petri dishes cultured with *S. aureus* and *E. coli*. The dishes were then incubated at 37 °C for 24 hours, and the inhibition zone area around each sample was calculated using Image J software. Three antimicrobial tests were performed on the individual sample.

2.5.2. Bacterial growth inhibition test. UV-treated samples (2 cm × 2 cm) were soaked in 9 mL of bacterial suspension and diluted at 1×10^4 cfu mL^{-1} using PBS solution. After co-culture on a shaking table at 37 °C for 24 h, 1 mL of mixed bacterial solution was coated on a Petri dish containing solid nutrient agar. The number of bacterial colonies on the plates was photographed and counted. All samples were tested in triplicate.

2.6. Electrical performance test

The Ag/Zn@PLA was placed in a Petri dish, and then 1 mL of phosphate-buffered saline (PBS) was added to wet the Ag/Zn@PLA sample. A multimeter measured the voltage and current of Ag/Zn@PLA dressing. The simulation of the electric field situation was implemented in the finite element-based Comsol Multiphysics software.[28]

2.7. Scratch wound assay

The test samples were sterilized by UV irradiation and placed in six-well plates and hanging transwell cell culture inserts (PIHT30R48T, Millipore) with the electrode facing downwards. HELF was inoculated into the lower chamber of a six-well plate. After the cells adhered to the monolayer, a straight line was drawn in the well with a 200 μL tip, rinsed three times with PBS, and 1 mL of DMEM/F-12 culture medium containing 2% fetal bovine serum was added and incubated in a 37 °C, 5% CO_2 incubator, and scratch healing was observed and photographed at 12 h and 24 h, respectively. Each group was repeated three times. Areas were calculated using Image J software. The cell migration rate (M%) was expressed as the change of the scratch area at different times and calculated using the equation: $M\% = (A_0 - A_t) \times 100\%/A_0$, where A_0 is the initial scratch area measured immediately after scratching and A_t is the scratch area measured at different times (t = 24 h) after scratching.

2.8. Cell cytotoxicity

Cell counting kit 8 (CCK-8) assay and fluorescence staining with calcein-AM/Propidium Iodide (PI) were performed to estimate the cytotoxicity of the samples. A detailed cytotoxic test process has been reported in our previous study.[14,27]

2.9. Animal experiments

Female C57BL/6 mice aged 6–8 weeks were purchased from SPF (Beijing) Biotechnology Co., Ltd. Divided C57 mice into three groups and raised in the SPF animal room of the Department of Medicine, Qingdao University. The Animal Experiment Committee of Qingdao University approved the animal experiment number QDU-AEC-AEC-2022490. The mice were fasted for 12 hours before surgery, the hair on the back of the mice was scraped with a razor, and the skin of the mice was disinfected by alcohol wiping. A round skin wound with a diameter of 0.8 mm was cut. UV-irradiated samples were placed on the wound surface. All samples were fixed with four stitches with surgical needles after band-aid bundling. Photographs of the wounds were taken on days 0, 3, 6, 9, and 12. Moreover, the wounds and surrounding skin tissues were removed and fixed in 4% paraformaldehyde for 24 hours. Then, the tissues were embedded in paraffin and stained with HE, Masson, and IHC (immunohistochemistry). The stained tissues were imaged with a sectioning scanner (C13239-01, Hamamatsu S210). For used Ag/Zn@PLA dressings, place the dressing contaminated with wound exudate in a container lined with a plastic bag impermeable to water and gas, add a special logo indicating it contains metal, and then transport the waste to the designated medical waste collection.

3. Results and discussion

3.1. Design and fabrication of Ag/Zn@PLA

After sputtering, a couple of circular Zn spot and Ag ring electrodes were integrated on the surface of the PLA nanofibrous membrane (Fig. 1a). The electrode area of Zn@PLA, Ag@PLA, and Ag/Zn@PLA was calculated at about 1.8%, 24.5%, and 26.3%, respectively (Fig. S1†). Considering that the density of Zn is 7.14 g cm^{-3} and the density of Ag is 10.53 g cm^{-3}, the weight ratio of Ag and Zn is about 20 : 1. Microscopically, the pristine PLA fiber surface is smooth and forms a highly interconnected porosity structure (Fig. 1b). An off-white and smooth coating (Ag

electrode) and a cellular coating (Zn electrode) were observed on the PLA fiber surface (Fig. 1b). The average diameter of PLA nanofiber was 0.79 ± 0.15 μm (Fig. 1c). Comparatively, the diameter of Ag-sputtered PLA and Zn-sputtered PLA nanofibers increased to 1.16 ± 0.23 μm and 1.34 ± 0.15 μm, respectively (Fig. 1c). The average pore sizes of PLA, Ag@PLA, Zn@PLA, and Ag/Zn@PLA were 5.3 μm, 4.7 μm, 4.3 μm, and 3.6 μm, respectively (Fig. 1d). In general, the Ag/Zn@PLA still possesses a porous morphological structure crucial for gaseous and fluid exchange in a wound environment. Moreover, the Ag/Zn elemental distribution determined by EDS indicated that the Ag and Zn coatings were uniformly encapsulated on the fiber surface (Fig. 1e). The digital photo, SEM observation, diameter increase, and EDS mapping confirmed that Ag/Zn coating was successfully sputtered on PLA fibers.

3.2. Physical and chemical characterization of Ag/Zn@PLA

The thermal stability and Ag/Zn content of Ag/Zn@PLA were investigated by thermogravimetric analysis. Fig. 2a shows that the degradation behaviors of PLA, Ag@PLA, Zn@PLA, and Ag/Zn@PLA are almost similar, and all had distinct peaks between 280 and 367 °C, attributing to the decomposition of PLA.[29,30] The residual weights of Ag@PLA, Zn@PLA, and Ag/Zn@PLA are higher than PLA, which can be attributed to the weight of Ag or Zn coating (Fig. 3b). Based on the weight difference, the deposited Ag/Zn content can be calculated at ~5.43 wt% and 0.83 wt%, respectively.

Hydrophilicity is one of the vital properties of wound dressings.[31,32] The WCA of pure PLA nanofibrous membrane is ~130° (Fig. 2c) due to PLA containing many hydrophobic ester groups. The typical hydrophobic character of PLA is beneficial for preventing bacterias adherence to the wound outside.[33,34] After sputtering, Ag@PLA showed a WCA of ~127°, whereas Zn@PLA showed 52°. The Zn coating improved the hydrophilicity of the PLA nanofibrous membrane, benefiting the wetness of the Ag/Zn electrodes and the adhesion of fibroblast cells.

Appropriate mechanical properties and flexibility are preconditions for wound dressings.[35,36] Typical stress–strain curves were similar during Ag@PLA, Zn@PLA, and Ag/Zn@PLA's stretching (Fig. 2d). After spurting, Young's modulus (Fig. 2e) and tensile strength (Fig. 2f) of PLA nanofibrous membrane increased, which can be explained by the stress distribution as Ag/Zn dots increased fiber interaction. Moreover, the Ag/Zn coating would not reduce the flexibility of PLA, confirming the excellent fitness of Ag/Zn@PLA on irregular wounds.

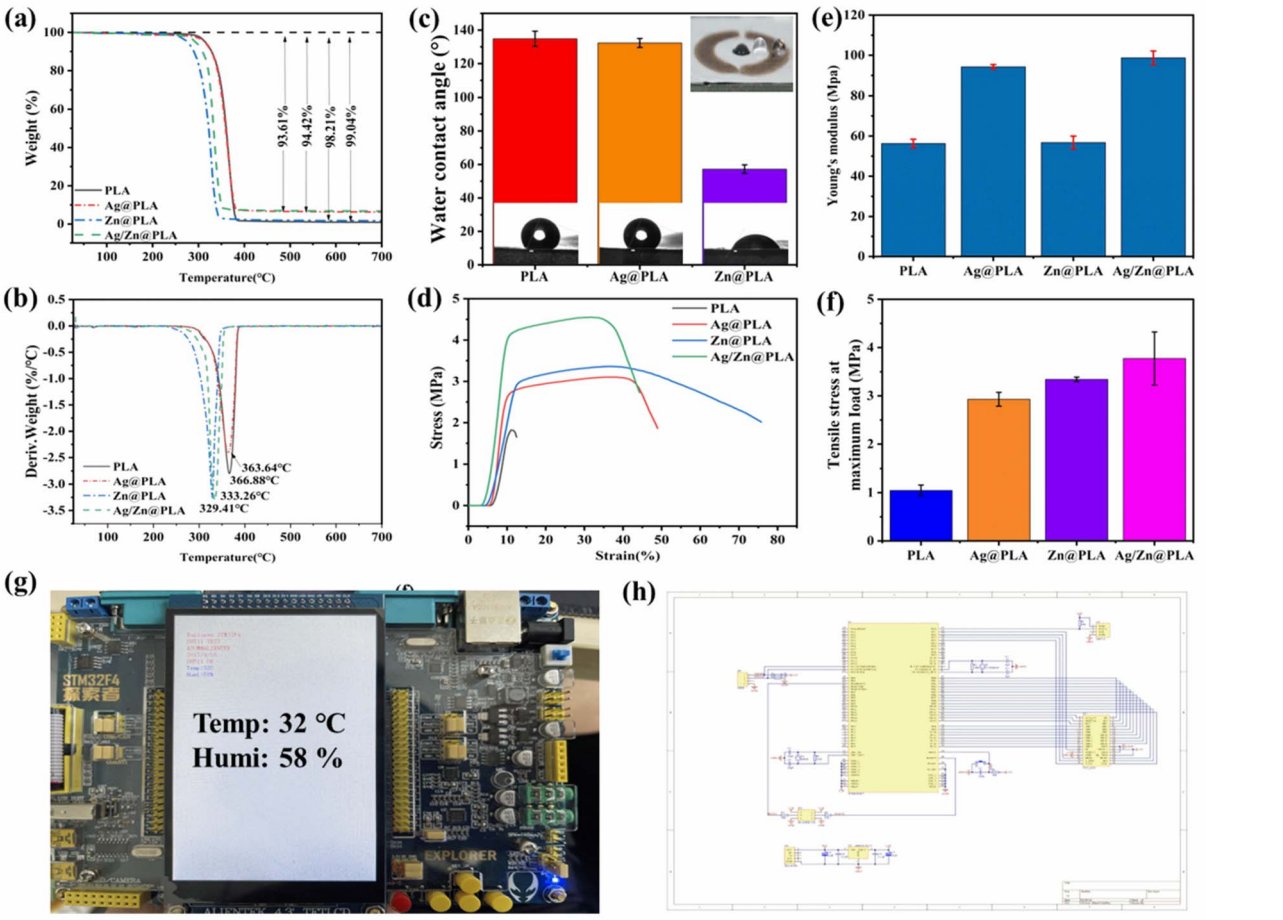

Fig. 2 (a) Thermogram and (b) DTG curves of PLA, Ag@PLA, Zn@PLA, and Ag/Zn@PLA. (c) The contact angle of PLA, Ag@PLA, and Zn@PLA. (d) The stress–strain curves of PLA, Ag@PLA, and Zn@PLA. (e) Young's modulus and (f) tensile strength of PLA, Ag@PLA, and Zn@PLA. (g) Single-chip monitor displays temperature obtained by a temperature sensor. (h) Schematic circuit diagram of the dressing device.

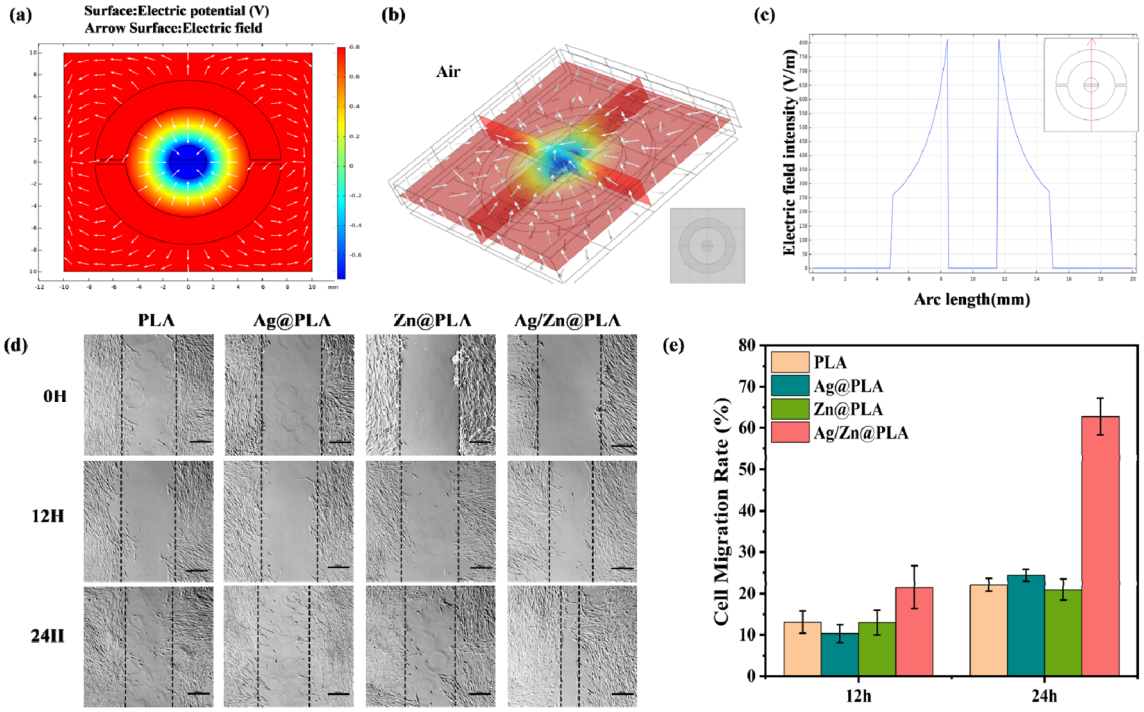

Fig. 3 (a) The electrical field of Ag/Zn@PLA was simulated by finite element software COMSOL in a two-dimensional plane. (b) The electrical field of Ag/Zn@PLA was modeled and simulated by finite element software COMSOL in a three-dimensional plane. (c) Detailed electric field intensity. Truncation started from $x = 0$, $y = -10$, and ended at $x = 0$, $y = 10$. (d) Representative images show cell migration at 12 and 24 h after scratching. (e) The cell migration rate of different samples treated fibroblasts.

To monitor the wound temperature in real-time, a miniature sensor Dht11 was attached to the Ag/Zn@PLA dressing using medical adhesive plaster, and Dht11 and STM32F407 monolithic microcomputers were connected with leads. The information measured by Dht11 was transmitted to a monolithic microcomputer through leads, and the wound temperature was displayed using the display screen of a monolithic microcomputer (Fig. 2g). The circuit design is shown in Fig. 2h.

3.3. Electric activity and cell migration of Ag/Zn@PLA

The endogenous electric field (EF) is thought to play an important role in promoting the directional migration of epidermal cells to the center.[37,38] When a wound that disrupts the epithelial barrier occurs, the wound surface immediately generates an EF pointing from the edge to the center.[39,40] When Ag/Zn@PLA dressings come into contact with blood or wound extrusions, a set of redox reactions between the Ag and Zn electrodes are expected to occur:[41,42]

Ag electrode:

$$Ag_2O + H_2O + 2e^- \rightarrow 2Ag + 2OH^- \quad (1)$$

Zn electrode:

$$Zn - 2e^- + 2OH^- \rightarrow Zn(OH)_2 \quad (2)$$

Based on the above equations, the Ag cathode undergoes a reduction process, and the Zn anode undergoes oxidation, resulting in a DC voltage. The finite element simulation showed that the EF generated from the Ag electrode towards the Zn electrode (Fig. 3a and b) could enhance the endogenous EF from the edge to the center of the wound. Moreover, the EF intensity was vigorous near the Ag/Zn electrodes (Fig. 3a and b). The simulated electric field intensity was 800 mV mm^{-1} (Fig. 3c), while the measured peak voltage of Ag/Zn@PLA was ~140 mV (Fig. S2†), which can be attributed to the different conductivity, electrostatic constant, and some irrational characteristics of the electrochemical system.[43] Theoretically, wound healing would be accelerated as Ag/Zn@PLA can generate an EF with a similar direction to the wound's endogenous EF.

Furthermore, an *in vitro* scratch-wound healing assay was performed to evaluate the Ag/Zn@PLA's potential to promote cell migration. The photographs were collected for 12 h and 24 h (Fig. 3c), and the cell migration rate was analyzed (Fig. 3d). At 12 hours, the cell migration rate of the Ag/Zn@PLA group was 22.3%, while the other groups were close to 10%. At 24 hours, the cell migration rate of the Ag/Zn@PLA group was 63.4%, which was significantly higher than those of the PLA group, Ag@PLA, and Zn@PLA groups. The results confirmed that the ES generated by Ag/Zn@PLA could significantly promote the migration of fibroblasts, confirming its pro-wound healing potential.

3.4. Antibacterial performance of Ag/Zn@PLA

Bacterial infection has been one of the significant obstacles in wound healing.[44,45] Thus, effectively inhibiting bacterial growth is essential for wound dressings.[46] Firstly, the agar plate

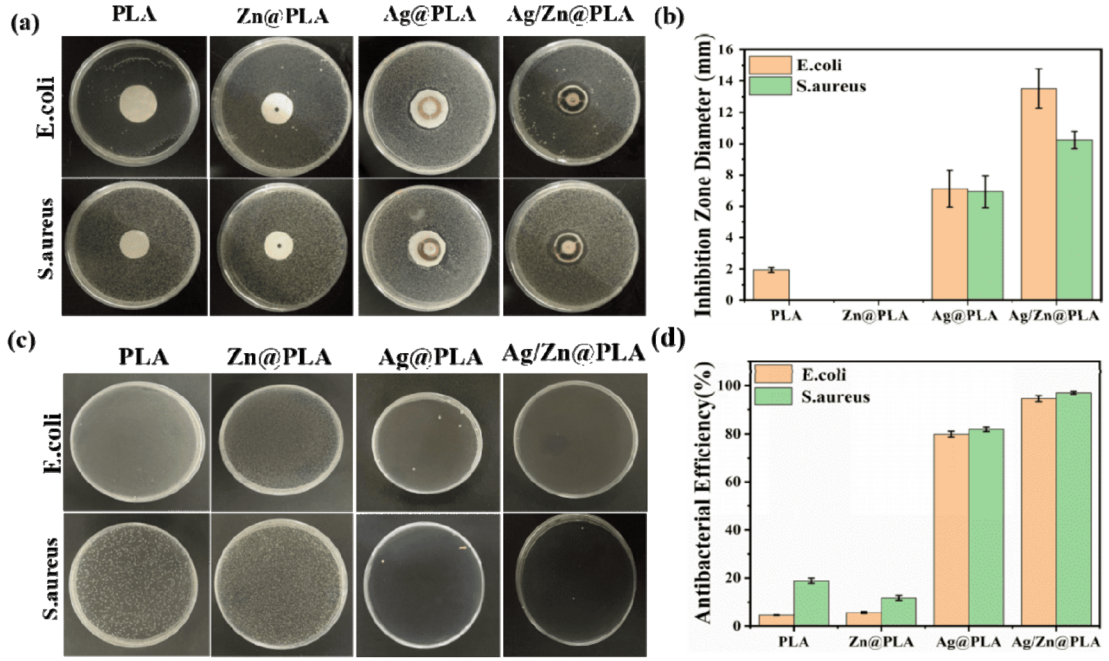

Fig. 4 Antimicrobial activity analysis. (a) Photograph of the agar plate in the disk diffusion method. (b) Inhibition zone diameters of different samples. (c) Photographs of colonies in the bacterial growth inhibition test. (d) Antimicrobial efficiency of different samples.

diffusion method tested the antibacterial property of Ag/Zn@PLA against *S. aureus* and *E. coli*. As shown in Fig. 4a, pure PLA did not produce inhibition zones, indicating that pure PLA does not have any antibacterial activity. In contrast, obvious inhibition zones were observed for the Ag@PLA and Ag/Zn@PLA (Fig. 4a). The inhibition zone diameter of Ag/

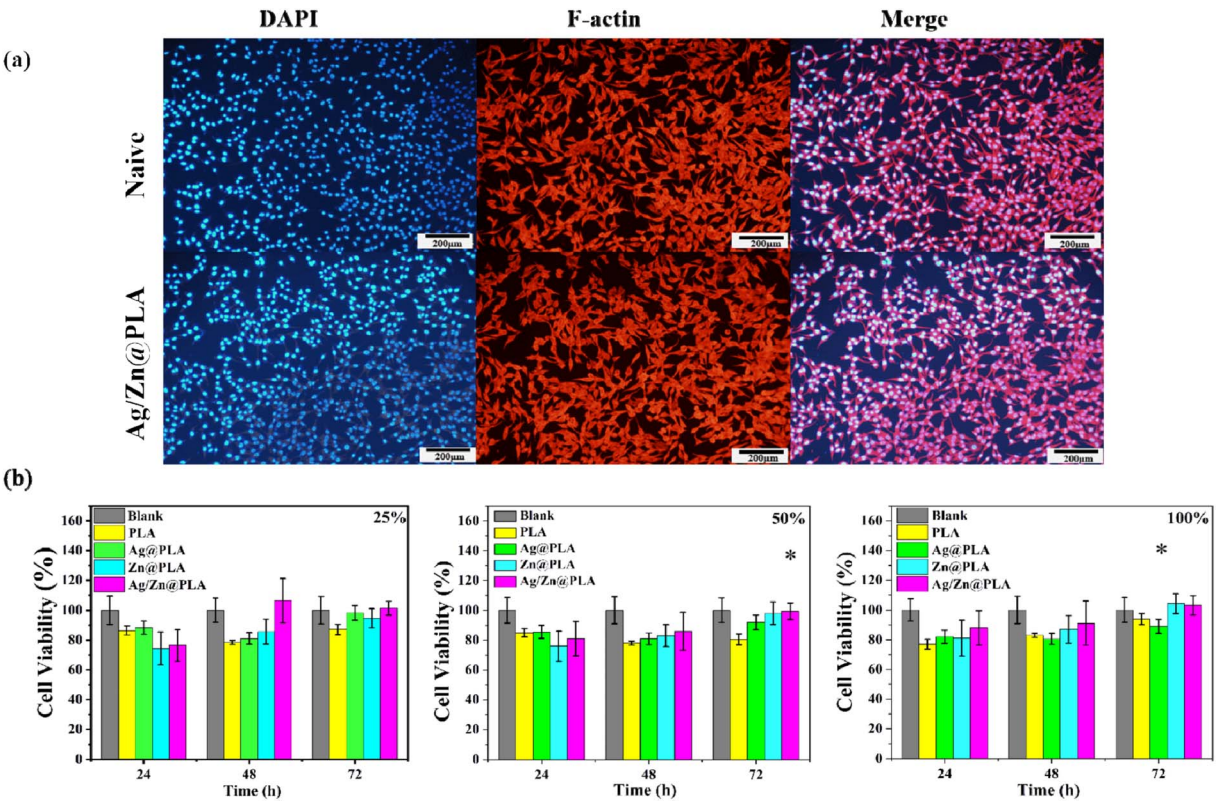

Fig. 5 (a) Fluorescence images of fibroblast cells co-cultured with various samples for 48 h. (b) Cell viability was determined by CCK-8 assay for different sample extracts after 24, 48, and 72 h incubation.

Zn@PLA could reach 12.43 ± 0.42 mm for *E. coli* and 9.76 ± 0.32 mm for *S. aureus* (Fig. 4b), respectively. Since the Zn electrode is in the middle of Zn@PLA, making Zn^{2+} challenging to release into the medium and generate an inhibition zone. Furthermore, the antibacterial performance was quantified by the colony counting method. It was found that the bacterial colony number decreased evidently in Ag/Zn@PLA (Fig. 4c), with the antibacterial efficiency of *E. coli* and *S. aureus* as high as 95 ± 4.7% and 97 ± 3.5%, respectively (Fig. 4d). The excellent antibacterial activity of Ag/Zn@PLA can be attributed to the

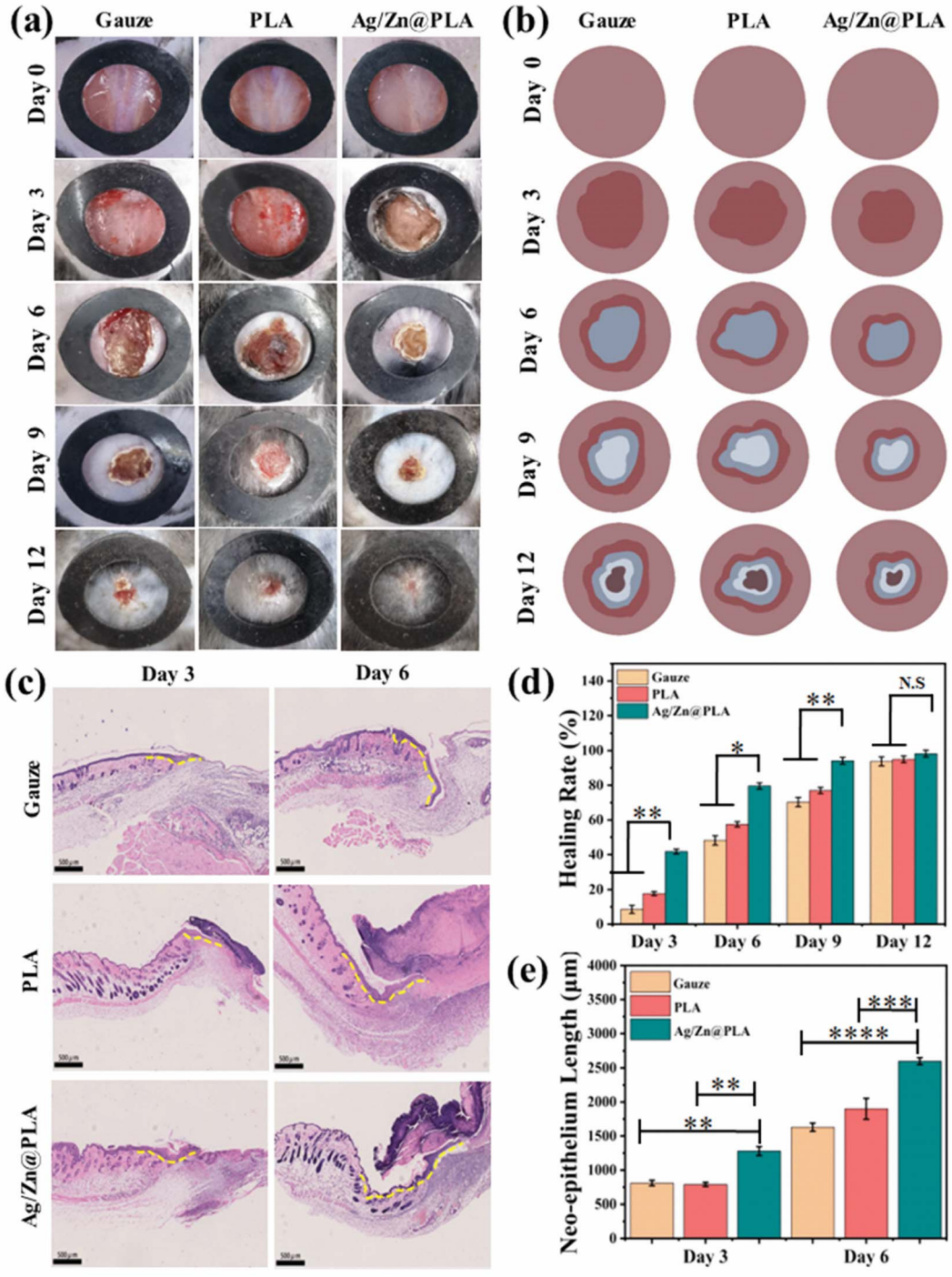

Fig. 6 *In situ* evaluation of Ag/Zn@PLA in promoting wound healing. (a) Representative photographs of rat wounds in different treatment groups on postoperative days 0, 3, 6, 9, and 12. (b) Illustrations of the mice wound areas on postoperative days 0, 3, 6, 9, and 12. (c) Representative H&E staining images and the yellow dashed line indicated the length of the new wound (the scale bar is 500 μm). (d) Healing rate in the different groups on postoperative days 3, 6, 9, and 12. (e) Statistics of new epithelium length in the wound on postoperative days 3 and 6. N.S, $p > 0.05$, *$p < 0.05$, **$p < 0.01$, ***$p < 0.001$, ****$p < 0.0001$. $n = 3$.

synergistic effect of electrical stimulation and the continuous release of Ag^{+}/Zn^{2+}.[26,47]

3.5. Biocompatibility of Ag/Zn@PLA

Because the dressings are in direct contact with wound tissue, acceptable cytotoxicity is required for their clinical application.[48–50] The morphology of fibroblast cells cultured on different samples was observed using an inverted fluorescence microscope. F-actin was stained with rhodamine-phalloidin (red), and nuclei were counterstained with DAPI solution (blue). As shown in Fig. 5a, fibroblast cells present normal cell morphological structures, with red F-actin and blue nuclei well dispersed on the samples' surface. Moreover, given the extensive overlap between F-actin and the nucleus, the fibroblast cells have active metabolic functions and remain healthy. Moreover, the proliferation of cells was evaluated by CCK-8 analysis. After incubation for 24, 48, and 72 h, there was no statistical difference in the cell viability of fibroblast culture in the different extract concentrations of PLA, Ag@PLA, Zn@PLA, and Ag/Zn@PLA (Fig. 5b). These results confirmed that the Ag/Zn@PLA had good biocompatibility with negligible cytotoxicity *in vitro*.

3.6. Wound healing *in vivo* of Ag/Zn@PLA

The Ag/Zn@PLA exhibits good physicochemical properties, outstanding antibacterial performance, high cell migration-promoting activity, and excellent biocompatibility, making it a wonderful candidate for wound healing. Therefore, a full-thickness skin incision model was further employed to confirm the feasibility of using Ag/Zn@PLA in real wound healing applications. The incision was covered with gauze as a control group.

3.6.1. Wound closure and new epithelialization. The photographs of the wound appearance and the traces of wound closure are shown in Fig. 6a and b. From day 3 onwards, the Ag/Zn@PLA group showed a faster healing tendency than the PLA and gauze groups. On day 6 after treatment, the healing rate of the Ag/Zn@PLA group was 79.6 ± 1.8%, while the healing rate of the PLA group and gauze group was only 57.5 ± 1.6% and 48.2 ± 2.7%, respectively ($p < 0.05$). On the 12th day, the wound of the Ag/Zn@PLA group almost disappeared, but the PLA group and the gauze group still had ~5% and ~7% left, respectively. At the same treatment time, the Ag/Zn@PLA group showed the best healing rate, suggesting the wound healing promotion performance of Ag/Zn@PLA. Moreover, the formation of new epithelium in the wound site was evaluated by HE staining (Fig. 6c). After treatment for day 3, the new epithelium length for the Ag/Zn@PLA, PLA, and gauze groups was 1299 ± 84 μm, 903 ± 67 μm, and 868 ± 83 μm, respectively. Consistent with the wound healing rate, after 6 days, although the new epithelium length for all groups still increased, the Ag/Zn@PLA group was significantly higher than that in the other two groups ($p < 0.01$), showing the best ability of epidermis formation. This can be attributed to the Ag/Zn electrodes generated ES and Zn^{2+}, stimulating epithelial formation during wound healing.[51,52]

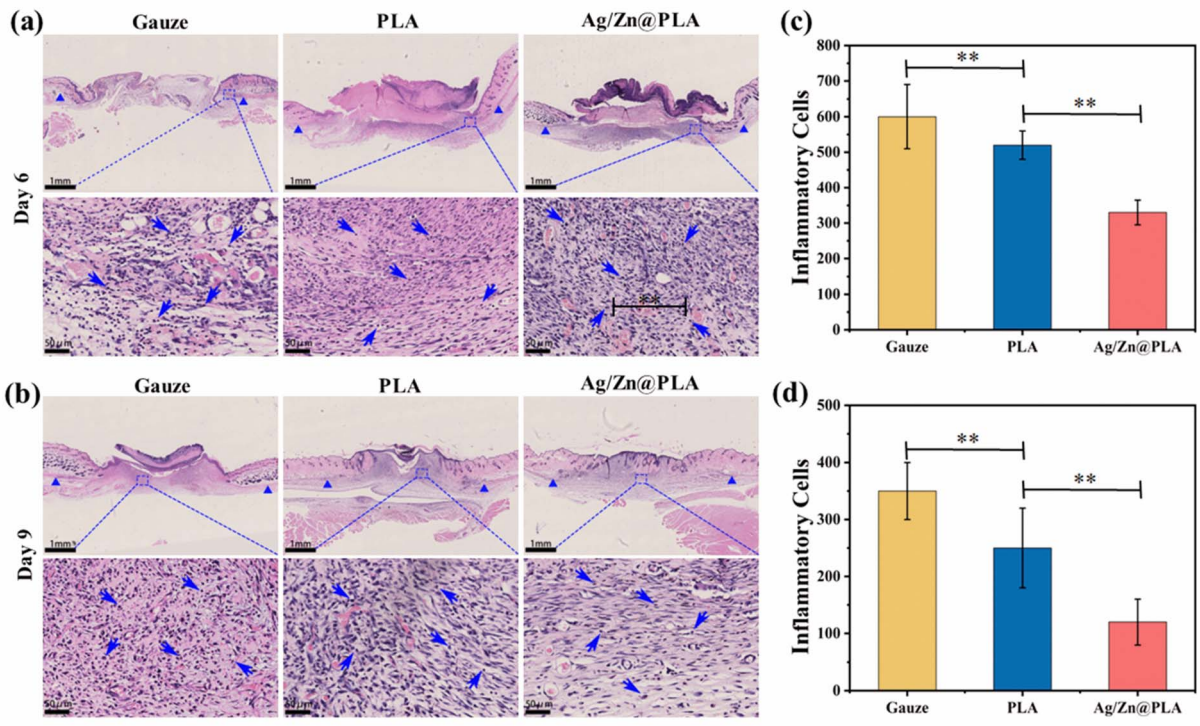

Fig. 7 (a) HE staining of tissue sections from mice healed for 6 days, blue triangles indicate the junction between the wound and normal skin, and blue arrows indicate inflammatory cells. (b) Number of inflammatory cells after healing for 6 days. (c) HE staining of tissue sections from mice healed for 9 days, with blue dashed lines indicating the junction between the wound and normal skin and blue arrows indicating inflammatory cells. (d) Number of inflammatory cells at 9 days of healing.

3.6.2. Inflammatory reaction. Severe inflammatory response and infiltration of inflammatory cells can delay wound healing.[53,54] The wound site skin was taken for HE staining on days 6 and 9 to observe the inflammatory cell infiltration (Fig. 7a and c). As shown in Fig. 7b, after treatment for 3 days, the inflammatory cells in the wound treated by the Ag/Zn@PLA (353 ± 28) were significantly less than those in the PLA (520 ± 28) and gauze-treated groups (602 ± 56) ($p < 0.01$). Moreover, on day 9, the inflammatory cell infiltration in the Ag/Zn@PLA treated group was still significantly lower than those of the PLA and gauze-treated groups ($p < 0.01$) (Fig. 7d). In general, the Ag/Zn@PLA positively inhibited the infiltration of inflammatory cells in the wound.

3.6.3. Neovascularization and collagen deposition. Neovascularisation plays an essential role in the later stage of wound healing.[55,56] Immunohistochemical staining for CD31, a vascular endothelial cell differentiation and maturation marker, was used to evaluate neovascularization formation at the wound site. As shown in Fig. 8a, the Ag/Zn@PLA group has the highest vessel density. In addition, the quantitative analysis demonstrated that Ag/Zn@PLA increased the vessel area most obviously (19.1 ± 2.65%), compared with the PLA group (4.67 ± 2.52%) and control group (1.1 ± 1.73%) (Fig. 8b). The results indicated that the Ag/Zn@PLA could actively promote the formation of new capillaries during wound healing. In addition, the collagen content of the new skin tissue was evaluated by Masson staining. At the end of the healing process (after 12 days of treatment), the Ag/Zn@PLA exhibited a more extensive, darker color and denser collagen deposition than the PLA and control groups (Fig. 8c). Furthermore, the quantitative analysis showed that the collagen fiber area percentage was 86.12 ± 2.59% in the Ag/Zn@PLA group, which was significantly higher ($P < 0.05$ and 0.001) compared to the PLA (50.35 ± 2.26%) and the control group (36.37 ± 3.89%) (Fig. 8d). The results showed that Ag/Zn@PLA could promote the formation of collagen.

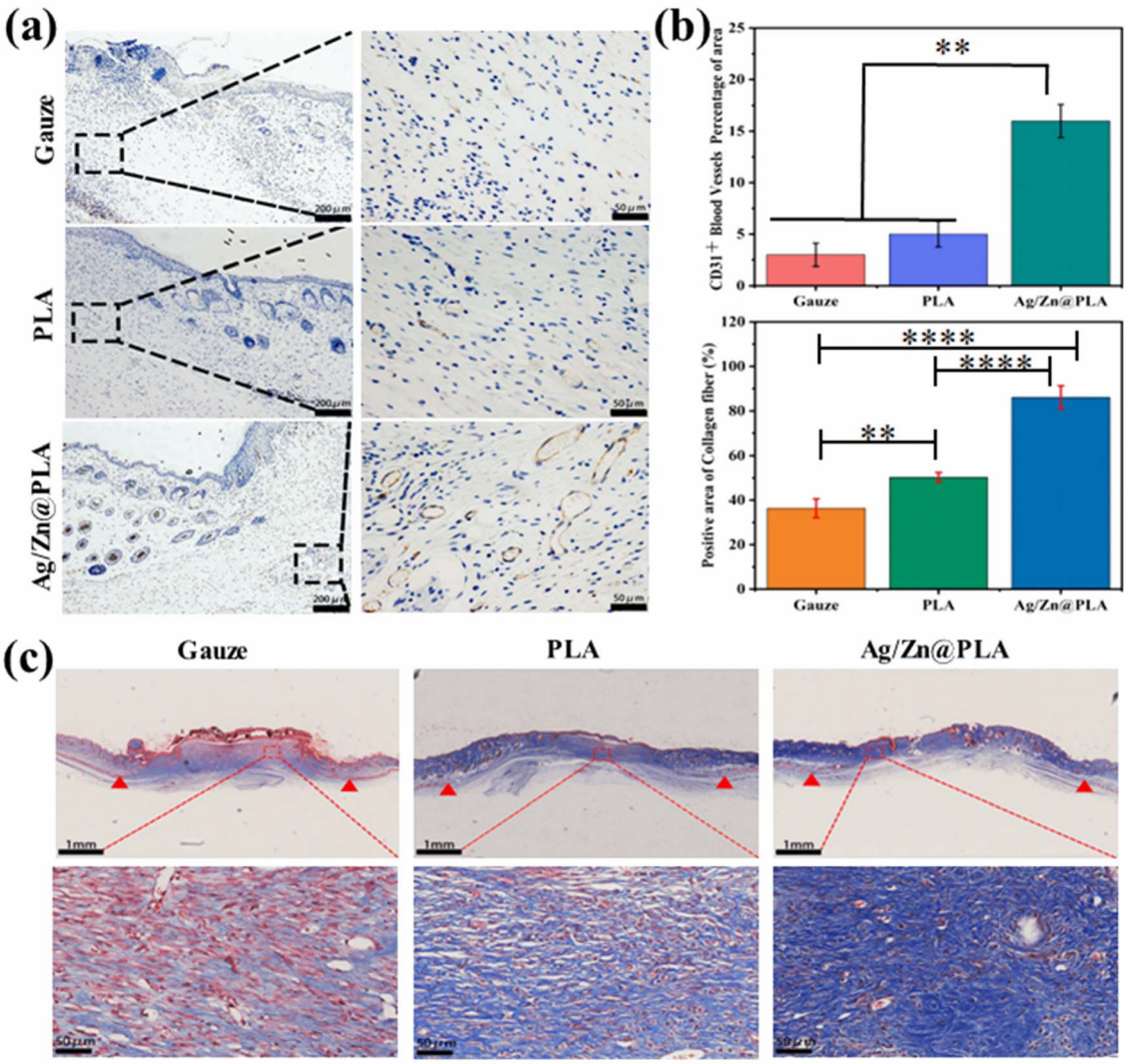

Fig. 8 (a) Immunohistochemical staining for CD31 in tissue sections from mice healed for 12 days. (b) Number and percentage of CD31 + cells. (c) Masson staining of tissue sections from mice healed for 12 days, with red triangles indicating the junction between the wound and normal skin (**$p < 0.01$, ***$p < 0.001$. $n = 3$.)

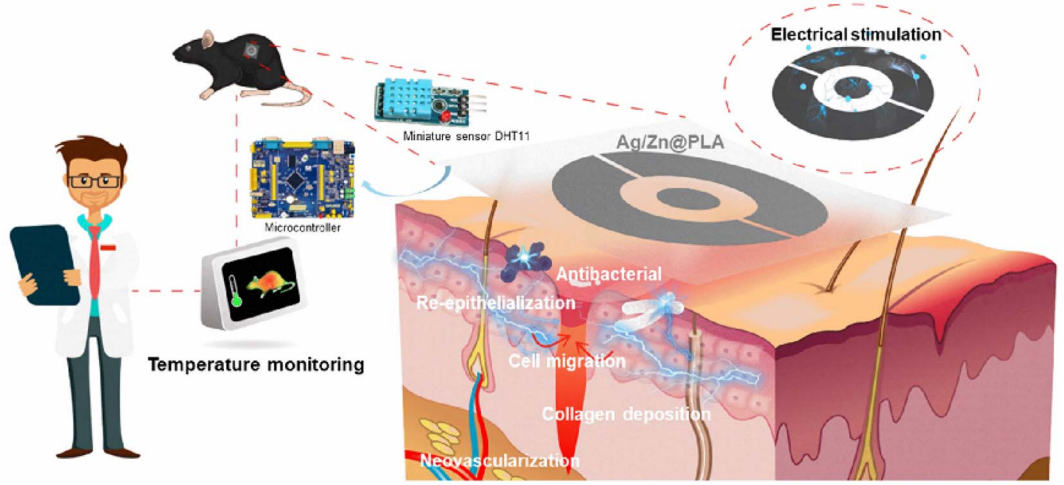

Fig. 9 Illustration of the possible wound healing promoting mechanism of Ag/Zn@PLA with miniature temperature sensor.

Previous studies have reported that many factors influence wound temperatures, such as bacterial infection, inflammation, new tissue formation, and remodeling.[57,58] Temperature is a particularly worthwhile parameter for real-time monitoring of wound status. With the help of an integrated sensing system, Ag/Zn@PLA can reveal real-time temperature fluctuation during wound healing. The wound temperature peaked at 33.5 °C on day 3, then decreased and finally showed an increasing trend after day 6 (Fig. S3†). Moreover, the temperature-changing trend is consistent with the infrared thermometer test results (Fig. S4†). The normal inflammatory response may cause the temperature peak on day 2, and the increasing trend after day 6 may be related to angiogenesis and new tissue formation. With the development of intelligence and the further optimization of sensor materials, real-time temperature monitoring of the wound will be possible.

3.6.4. Wound healing mechanism. Based on the physicochemical, electric activity, antibacterial, cell, animal, and histological analyses, the proposed wound healing mechanisms of Ag/Zn@PLA can be summarized as follows: (1) the nanofibrous PLA membrane can provide a biomimetic extracellular matrix for cell proliferation, accelerating the growth of new epidermis. (2) The released Ag^{+}/Zn^{2+} could kill bacteria in the wound, inhibiting inflammatory cell infiltration and preventing wound infection. (3) The Ag/Zn generated electrical stimulation could promote cell migration, collagen deposition, and neovascularization, accelerating wound healing. (4) Combined with the miniature sensor, Ag/Zn@PLA can monitor the wound temperature and provide early warning of wound infection (Fig. 9). Combining hydro-activated electrotherapy activity and temperature monitoring may provide a novel integrated strategy for wound healing.

4. Conclusions

In conclusion, a novel electroactive nanofibrous dressing (Ag/Zn@PLA) was prepared by magnetron sputtering. The Ag/Zn@PLA dressing showed excellent antibacterial activity against *Escherichia coli* and *Staphylococcus aureus*. Meanwhile, the electrical stimulation generated by Ag/Zn electrodes could facilitate the migration of fibroblasts and further promote wound re-epithelialization, collagen fiber deposition, and neovascularization. Moreover, combined with the miniature sensor, the Ag/Zn@PLA can monitor the wound temperature and provide early warning of wound infection. Importantly, the Ag/Zn@PLA exhibited good biocompatibility. This study demonstrated that electroactive nanofibrous dressing with temperature monitoring could be an excellent candidate for skin wound healing.

Conflicts of interest

There are no conflicts to declare.

Acknowledgements

This work was partially supported by the National Natural Science Foundation of China (52203060), the Shandong Provincial Universities Youth Innovation Technology Plan Innovation Team (2022KJ152), and the Postdoctoral Research Foundation of China (2022M711735).

References

1 Y. Yang, Y. Du, J. Zhang, H. Zhang and B. Guo, *Adv. Fiber Mater.*, 2022, **4**, 1027–1057.
2 C. Wang, Y. Liang, Y. Huang, M. Li and B. Guo, *J. Mater. Sci. Technol.*, 2022, **121**, 207–219.
3 K. Wu, Q. Yang, L. Zhang, P. Xu, X. Wu, H. Yang, H. Zhou, X. Lin and L. Yang, *J. Mater. Sci. Technol.*, 2023, **133**, 123–134.
4 L. Yu, H. Zhang, L. Xiao, J. Fan and T. Li, *ACS Appl. Mater. Interfaces*, 2022, **14**, 21814–21821.
5 J. Liang, H. Zeng, L. Qiao, H. Jiang, Q. Ye, Z. Wang, B. Liu and Z. Fan, *ACS Appl. Mater. Interfaces*, 2022, **14**, 30507–30522.

6 R. Luo, J. Dai, J. Zhang and Z. Li, *Adv. Healthcare Mater.*, 2021, **10**, 2100557.
7 J. He, Y. Liang, M. Shi and B. Guo, *Chem. Eng. J.*, 2020, **385**, 123464.
8 Z. Song, J. Wang, S. Tan, J. Gao and L. Wang, *Colloids Surf., A*, 2023, **656**, 130211.
9 X. Jin, Y. Shang, Y. Zou, M. Xiao, H. Huang, S. Zhu, N. Liu, J. Li, W. Wang and P. Zhu, *ACS Appl. Mater. Interfaces*, 2020, **12**, 56681–56691.
10 C. Korupalli, H. Li, N. Nguyen, F.-L. Mi, Y. Chang, Y.-J. Lin and H.-W. Sung, *Adv. Healthcare Mater.*, 2021, **10**, 2001384.
11 Z. Zhou, J. Wang, J. Zhang, X. Duan, W. Lin, K. Cheng, W. Weng and Z. Chen, *Colloids Surf., B*, 2022, 112980, DOI: 10.1016/j.colsurfb.2022.112980.
12 X. Shi, Y. Chen, Y. Zhao, M. Ye, S. Zhang and S. Gong, *Biomater. Sci.*, 2022, **10**, 692–701.
13 *Antioxid. Redox Signaling*, 2020, **33**, 713–724.
14 H. Dong, S. Zhang, L. Yang, N. Wang, S. Chen, J. Ma and J. Li, *Composites, Part B*, 2021, **224**, 109240.
15 S. Ghatak, D. K. Khona, A. Sen, K. Huang, G. Jagdale, K. Singh, V. Gopalakrishnan, K. G. Cornetta, S. Roy, S. Khanna, L. A. Baker and C. K. Sen, *Sci. Rep.*, 2021, **11**, 21723.
16 C. Yu, Z.-X. Xu, Y.-H. Hao, Y.-B. Gao, B.-W. Yao, J. Zhang, B. Wang, Z.-Q. Hu and R.-Y. Peng, *Mil. Med. Res.*, 2019, **6**, 22.
17 S. Liu, J. Li, S. Zhang, X. Zhang, J. Ma, N. Wang, S. Wang, B. Wang and S. Chen, *ACS Appl. Bio Mater.*, 2020, **3**, 848–858.
18 S. Tan, Z. Huang, J. Wang, J. Han, J. Gao and L. Wang, *Text. Res. J.*, 2021, **91**, 2345–2356.
19 A. Raman, J. S. Jayan, B. D. S. Deeraj, A. Saritha and K. Joseph, *Surf. Interfaces*, 2021, **24**, 101140.
20 X. Xie, Y. Chen, X. Wang, X. Xu, Y. Shen, A. u. R. Khan, A. Aldalbahi, A. E. Fetz, G. L. Bowlin, M. El-Newehy and X. Mo, *J. Mater. Sci. Technol.*, 2020, **59**, 243–261.
21 G. Augustine, M. Aarthy, H. Thiagarajan, S. Selvaraj, N. R. Kamini, G. Shanmugam and N. Ayyadurai, *Adv. Healthcare Mater.*, 2021, **10**, 2001832.
22 W. Liang, M. Jiang, J. Zhang, X. Dou, Y. Zhou, Y. Jiang, L. Zhao and M. Lang, *J. Mater. Sci. Technol.*, 2021, **89**, 225–232.
23 K. Wu, X. Wu, J. Guo, Y. Jiao and C. Zhou, *Adv. Healthcare Mater.*, 2021, **10**, 2100793.
24 Z. Zhang, R. Su, F. Han, Z. Zheng, Y. Liu, X. Zhou, Q. Li, X. Zhai, J. Wu, X. Pan, H. Pan, P. Guo, Z. Li, Z. Liu and X. Zhao, *RSC Adv.*, 2022, **12**, 3243–3252.
25 D. Lou, Q. Pang, X. Pei, S. Dong, S. Li, W.-q. Tan and L. Ma, *Biosens. Bioelectron.*, 2020, **162**, 112275.
26 Y. Feng, N. Wang, T. He, R. He, M. Chen, L. Yang, S. Zhang, S. Zhu, Q. Zhao, J. Ma, S. Chen and J. Li, *ACS Appl. Mater. Interfaces*, 2021, **13**, 59196–59205.
27 Y. Cheng, J. Li, M. Chen, S. Zhang, R. He and N. Wang, *Sep. Purif. Rev.*, 2022, **294**, 121165.
28 O. Wahlsten, J. B. Skiba, I. R. S. Makin and S. P. Apell, *J. Electr. Bioimpedance*, 2016, **7**, 13–19.
29 Q. Li, X. Hu, P. Perkins and T. Ren, *Int. J. Biol. Macromol.*, 2022, **224**, 848–857.
30 Q. Deng, F. Wang, C. R. Gough and X. Hu, *Int. J. Biol. Macromol.*, 2022, **197**, 55–67.
31 H. Donya, R. Darwesh and M. K. Ahmed, *Int. J. Biol. Macromol.*, 2021, **186**, 897–908.
32 A. Zhou, Y. Zhang, X. Zhang, Y. Deng, D. Huang, C. Huang and Q. Qu, *Int. J. Biol. Macromol.*, 2022, **201**, 448–457.
33 J. Yin, L. Xu and A. Ahmed, *Adv. Fiber Mater.*, 2022, **4**, 832–844.
34 B. Kost, M. Svyntkivska, M. Brzeziński, T. Makowski, E. Piorkowska, K. Rajkowska, A. Kunicka-Styczyńska and T. Biela, *Colloids Surf., B*, 2020, **190**, 110949.
35 S. Sun, M. Hao, C. Ding, J. Zhang, Q. Ding, Y. Zhang, Y. Zhao and W. Liu, *Colloids Surf., B*, 2022, **217**, 112692.
36 J. Liu, Z. Zheng, J. Luo, P. Wang, G. Lu and J. Pan, *Colloids Surf., B*, 2022, 112987, DOI: 10.1016/j.colsurfb.2022.112987.
37 J. Yang, X. Liu, W. Wang, Y. Chen, J. Liu, Z. Zhang, C. Wu, X. Jiang, Y. Liang and J. Zhang, *Bioelectrochemistry*, 2022, **148**, 108247.
38 C. K. Nanditha and G. S. V. Kumar, *Mater. Today*, 2022, **14**, 100235.
39 Y. Liang, H. Tian, J. Liu, Y. Lv, Y. Wang, J. Zhang and Y. Huang, *Bioelectrochemistry*, 2020, **135**, 107578.
40 Z. Wang, W. You, W. Wang, W. Tian, F. Chen, Y. Xiao, Y. Chen and X. Wang, *Adv. Fiber Mater.*, 2022, **4**, 6.
41 D. K. Khona, S. Roy, S. Ghatak, K. Huang, G. Jagdale, L. A. Baker and C. K. Sen, *Bioelectrochemistry*, 2021, **142**, 107921.
42 O. Gotlib, S. Vaitkus, R. Simoes-Torigoe, K. Morris, A. Bodnar, F. E. Spada, M. Alagiri and F. E. Talke, *J. Mater. Res.*, 2021, **10**, 339–348.
43 Y.-K. Won, C. B. Lin, M. Seiberg, N. Chen, Y. Hu, D. Rossetti, C. Saliou and C.-J. Loy, *Arch. Dermatol.*, 2014, **306**, 27–35.
44 X. Zhang, R. Lv, L. Chen, R. Sun, Y. Zhang, R. Sheng, T. Du, Y. Li and Y. Qi, *ACS Appl. Mater. Interfaces*, 2022, **14**, 12984–13000.
45 F. N. Harandi, A. C. Khorasani, S. A. Shojaosadati and S. Hashemi-Najafabadi, *Surf. Interfaces*, 2022, **28**, 101592.
46 J. Chen, Z. Huang, H. Zhang, Z. Zhang, D. Wang, D. Xia, C. Yang and M. Dong, *Chem. Eng. J.*, 2022, **443**, 136234.
47 R. He, J. Li, M. Chen, S. Zhang, Y. Cheng, X. Ning and N. Wang, *J. Hazard. Mater.*, 2022, **428**, 128239.
48 J. Cai, B. Liu, W. Liu, L. Liu, Z. Fan and S. Lin, *Surf. Interfaces*, 2022, **30**, 101905.
49 X. Yang, L. Li, D. Yang, J. Nie and G. Ma, *Adv. Fiber Mater.*, 2020, **2**, 105–117.
50 Z. Zhang, T. Wang, S. Chen, C. Lv, X. Zhuang and S. Wang, *Surf. Interfaces*, 2022, **34**, 102392.
51 L. Feng, Q. Chen, H. Cheng, Q. Yu, W. Zhao and C. Zhao, *Adv. Healthcare Mater.*, 2022, **11**, 2201049.
52 W. Wentao, Z. Tao, S. Bulei, Z. Tongchang, Z. Qicheng, W. Fan, Z. Ninglin, S. Jian, Z. Ming and S. Yi, *Appl. Mater. Today*, 2019, **17**, 36–44.

53 M. Wang, J. Du, M. Li, F. Pierini, X. Li, J. Yu and B. Ding, *Biomater. Sci.*, 2023, **11**, 2383–2394.
54 Y. Sun, T. Miao, Y. Wang, X. Wang, J. Lin, N. Zhao, Y. Hu and F.-J. Xu, *Biomater. Sci.*, 2023, **11**, 2405–2418.
55 X. Wang, X. Tang, N. Li, Y. Sun, R. Yu, J. Zhang, D. Li, B. Yang and H. Sun, *Biomater. Sci.*, 2023, **11**, 235–247.
56 H. Cheng, Q. Yu, Q. Chen, L. Feng, W. Zhao and C. Zhao, *Biomater. Sci.*, 2023, **11**, 931–948.
57 N. Tang, Y. Zheng, D. Cui and H. Haick, *Adv. Healthcare Mater.*, 2021, **10**, 2101292.
58 M. Farahani and A. Shafiee, *Adv. Healthcare Mater.*, 2021, **10**, 2100477.